Journal of Computational Physics 229 (2010) 6135–6155

Contents lists available at ScienceDirect

Journal of Computational Physics

journal homepage: www.elsevier.com/locate/jcp

Three-dimensional, fully adaptive simulations of phase-field fluid models

Hector D. Ceniceros [a], Rudimar L. Nós [b,*], Alexandre M. Roma [c]

[a] Department of Mathematics, University of California, Santa Barbara, CA 93106, United States
[b] Departamento Acadêmico de Matemática, Universidade Tecnológica Federal do Paraná, CEP 80230-901, Curitiba, PR, Brazil
[c] Departamento de Matemática Aplicada, Universidade de São Paulo, Caixa Postal 66281, CEP 05311-970, São Paulo, SP, Brazil

ARTICLE INFO

Article history:
Received 28 September 2009
Received in revised form 22 April 2010
Accepted 27 April 2010
Available online 4 May 2010

Keywords:
Conservative phase-field models
Model H
Adaptive mesh refinements
Semi-implicit methods
Flow-induced drop coalescence
Kelvin–Helmholtz instability
Multi-level multigrid
Bharmonic equation

ABSTRACT

We present an efficient numerical methodology for the 3D computation of incompressible multi-phase flows described by conservative phase-field models. We focus here on the case of density matched fluids with different viscosity (Model H). The numerical method employs adaptive mesh refinements (AMR) in concert with an efficient semi-implicit time discretization strategy and a linear, multi-level multigrid to relax high order stability constraints and to capture the flow's disparate scales at optimal cost. Only five linear solvers are needed per time-step. Moreover, all the adaptive methodology is constructed from scratch to allow a systematic investigation of the key aspects of AMR in a conservative, phase-field setting. We validate the method and demonstrate its capabilities and efficacy with important examples of drop deformation, Kelvin–Helmholtz instability, and flow-induced drop coalescence.

1. Introduction

Fluid–fluid interfaces such as those bounding drops and bubbles are present in a large number of complex fluids such as emulsions, foams, and polymeric solutions which are found in a wide variety of industrial applications. The understanding of the dynamics of these systems is thus of significant scientific and technological interest. Numerical simulation can play an instrumental role toward aiding in achieving this goal. However, it is an outstanding computational challenge to accurately capture all the disparate time and length scales involved in these complex, nonlinear phenomena. Of course, this challenge is magnified for physically realistic three-dimensional computations.

In recent years conservative phase-field models have gained increased attention [1–11] as viable tools for the numerical investigation of multi-component flows. These are a particular type of diffuse-interface methods (see e.g. the review [12] and the references therein) in which fluid–fluid free boundaries are given a finite thickness. The idea of a diffuse interface [13–17] is compatible with the observation that physically there is a rapid but smooth transition of material properties across a fluid interface. In contrast, in a sharp interface model a free boundary is represented with zero thickness and the material properties are discontinuous across it.

The basic idea of the phase-field approach is to introduce an order parameter or phase field ϕ that varies continuously over a thin transition layer and is mostly uniform in the bulk phases. The models have an appealing variational-based formalism which facilitates the inclusion of different physical effects. In the conservative models, the evolution of ϕ is governed

* Corresponding author.
E-mail addresses: hdc@math.ucsb.edu (H.D. Ceniceros), rudimarnos@utfpr.edu.br (R.L. Nós), roma@ime.usp.br (A.M. Roma).
URLs: http://www.math.ucsb.edu/~hdc (H.D. Ceniceros), http://pessoal.utfpr.edu.br/rudimarnos (R.L. Nós), http://www.ime.usp.br/~roma (A.M. Roma).

0021-9991/$ - see front matter © 2010 Elsevier Inc. All rights reserved.
doi:10.1016/j.jcp.2010.04.045

by a fourth order equation of the Cahn–Hilliard type and due to a critical balance between nonlinear and diffusive terms, the solution's thin transition layer do not deteriorate dynamically. However, the numerical solution of these models is a daunting task. To their complex mathematical structure, characterized with high order derivatives and intricate nonlinearities, we must add the need to accurately resolve simultaneously the macroscopic flow and the extremely thin interfacial layer, as well as several time scales.

There have been recent advances in the numerical simulation of these models that include a Fourier spectral method [18], the design of implicit nonlinear multigrid methods [5,6], linear semi-implicit methods [3,21] and two-dimensional adaptive methods [11,19–21,26]. Here, we build on two of these recent works to develop, step by step, 3D, fully adaptive simulations for a phase-field model of an incompressible fluid with matched densities and variable viscosity, known as Model H according to the nomenclature of Hohenberg and Halperin [27]. The numerical methodology is based on the application of a linear semi-implicit time discretization combined with the projection method and using an accurate spatial discretization on adaptive mesh refinements [3,21]. The semi-implicit linear systems are solved at optimal cost with a multigrid approach. We also propose a scaling of surface tension that depends on the interfacial thickness and that appears to provide an appropriate calibration for similar phase field models. To our knowledge, the simulations presented here are one of the first fully adaptive 3D computations of Model H without the use of any public or commercial pre-built adaptive mesh modules. While revising this article, a finite element based, adaptive numerical method for 3D phase-field simulations was introduced by Zhou et al. [30]. Their adaptive method uses Delaunay mesh refinements and a fully implicit time discretization which is solved via Newton iterations.

The rest of the paper is organized as follows. We describe the model in Section 2 and devote Section 3 to discuss in detail the numerical approach. This is followed by a series of physically relevant numerical examples in Section 4 with which we validate and test the capabilities of the proposed methodology. Some final remarks are presented in Section 5.

2. The governing equations: Model H

We focus in this work on the conservative phase-field model that describes the coupling of a density matched, incompressible, binary mixture with a hydrodynamic flow. The system is described by an order parameter or phase field ϕ which is a measure of the relative composition or volume fraction of the two components and has an associated free energy given by

$$H[\phi] = \int_\Omega \left\{ \frac{1}{2}\alpha|\nabla\phi(\mathbf{x})|^2 + \beta f(\phi(\mathbf{x})) \right\} d\mathbf{x}, \tag{1}$$

where Ω is the region of space occupied by the system and α and β are constants. The gradient term accounts for the surface energy and $\beta f(\phi(\mathbf{x}))$ is the bulk energy density. To model two-phase flow, we choose f to be the double-well potential:

$$f(\phi) = \frac{1}{4}(1-\phi^2)^2. \tag{2}$$

The evolution of the order parameter is governed by the convective Cahn–Hilliard equation [28,29] which guarantees the conservation of the mean of ϕ:

$$\frac{\partial\phi}{\partial t} + \mathbf{u}\cdot\nabla\phi = \nabla\cdot[M(\phi)\nabla\mu(\phi)], \quad \mu(\phi) = \frac{\delta H[\phi]}{\delta\phi(\mathbf{x})}, \tag{3}$$

where $\mathbf{u}$ is the flow velocity, $M(\phi)$ is the mobility or Onsager coefficient and $\mu(\phi)$ is the chemical potential. In the absence of flow ($\mathbf{u}\equiv\mathbf{0}$), equilibrium states are characterized by $\mu(\phi)$ = constant. In addition to the two stable uniform states that correspond to $\phi(\mathbf{x})\equiv\pm1$, there is a one-dimensional equilibrium solution that characterizes the interfacial, transition layer and is given by (see e.g. [33])

$$\phi_0(z) = \tanh\left(\frac{z}{\sqrt{2}\xi}\right), \tag{4}$$

where

$$\xi = \sqrt{\frac{\alpha}{\beta}}. \tag{5}$$

Following [2], we define the interface thickness ϵ as the distance between $\phi = -0.9$ and $\phi = 0.9$. For the equilibrium interface, we have

$$\epsilon = 2\sqrt{2}\tanh^{-1}(0.9)\xi \approx 4.164\xi. \tag{6}$$

The conservation of momentum can be expressed in terms of the incompressible Navier–Stokes equations with the addition of a phase field-dependent surface force $\mu(\phi)\nabla\phi$ [34]:

$$\rho\left(\frac{\partial \mathbf{u}}{\partial t}+\mathbf{u}\cdot\nabla\mathbf{u}\right)=-\nabla p+\nabla\cdot[\eta(\phi)(\nabla\mathbf{u}+\nabla\mathbf{u}^T)]+\mu(\phi)\nabla\phi, \tag{7}$$

$$\nabla\cdot\mathbf{u}=0, \tag{8}$$

where ρ is the (constant) density, p is the pressure that enforces the incompressibility constraint (8), and $\eta(\phi)$ is the (concentration-dependent) viscosity. The coupled Cahn–Hilliard/Navier–Stokes system (3)–(8) is referred to as Model H [27]. We note that different phase-field models have been proposed for the case of variable density [35,36]. Many of the salient computational challenges of these models are also present in Model H. Thus, we believe that development of the computational methodology for this simpler model is an important step toward that required for the more elaborate phase-field models of multi-phase and complex fluids.

We nondimensionalize the Model H equations with the variables

$$\mathbf{u}'=\frac{\mathbf{u}}{U_c},\quad t'=\frac{t}{T_c},\quad \mathbf{x}'=\frac{\mathbf{x}}{L_c},\quad p'=\frac{pL_c}{\eta_c U_c}, \tag{9}$$

where L_c, U_c, T_c, and η_c are characteristic length, velocity, time, and viscosity, respectively. We select L_c to be the horizontal extent of the fluid domain and U_c will be taken in this work to be that of an imposed shear. Defining $T_c = L_c/U_c$, and dropping the primes we obtain

$$\frac{\partial\phi}{\partial t}+\mathbf{u}\cdot\nabla\phi=\frac{1}{Pe}\nabla\cdot[M(\phi)\nabla\mu(\phi)], \tag{10}$$

$$Re\left(\frac{\partial \mathbf{u}}{\partial t}+\mathbf{u}\cdot\nabla\mathbf{u}\right)=-\nabla p+\nabla\cdot[\eta(\phi)(\nabla\mathbf{u}+\nabla\mathbf{u}^T)]+\frac{1}{Ca}\mu(\phi)\nabla\phi, \tag{11}$$

$$\nabla\cdot\mathbf{u}=0, \tag{12}$$

where now $\eta(\phi)$ and $M(\phi)$ have been normalized by characteristic viscosity and mobility η_c and M_c, respectively, and μ has been scaled by β. The dimensionless groups used above are the Reynolds number, the capillary number, the Péclet number given by

$$Re=\frac{\rho U_c L_c}{\eta_c},\quad Ca=\frac{\eta_c U_c}{\beta L_c},\quad Pe=\frac{U_c L_c}{M_c\beta}, \tag{13}$$

respectively. The Reynolds number Re is the ratio between inertial and viscous forces and the capillary number Ca provides a measure of the relative magnitude of viscous and capillary (or interfacial tension) forces at the interface.

The Péclet number Pe is the ratio between the non-viscous diffusive time scale and the convective time scale. Naturally, we would like the phase-field flow to converge to the corresponding the sharp interface flow as $\epsilon\to 0$. Formally, this could be accomplished if $1/Pe$ goes to zero as $\epsilon\to 0$. Following Jacqmin [2] and Lee et al. [31], we take here $Pe = O(1/\epsilon)$. Other scalings have been proposed for different flow situations [32].

The surface tension σ for the phase-field model can be estimated from the flat, equilibrium interface to give [33]

$$\sigma=\frac{2\sqrt{2}}{3}\sqrt{\alpha\beta}. \tag{14}$$

Note from (5), (6) and (14) that the interface thickness is $O\left(\xi=\sqrt{\frac{\alpha}{\beta}}\right)$ and the surface tension is $O(\sqrt{\alpha\beta})$. Thus, surface tension will be $O(1)$ if we select $\alpha = O(\epsilon)$ and $\beta = O(1/\epsilon)$. Using (14) we can write Ca in terms of the surface tension as:

$$Ca=\frac{2\sqrt{2}}{3}\frac{\xi}{L_c}\frac{\eta_c U_c}{\sigma}. \tag{15}$$

Thus, for this phase-field model, the capillary number depends on the interface thickness. More precisely, defining the Cahn number K by

$$K=\frac{\xi}{L_c}, \tag{16}$$

which is a relative measure of the interface thickness, we can write Ca as

$$Ca=\frac{2\sqrt{2}K}{3}Ca^*, \tag{17}$$

where $Ca^* = \eta_c U_c/\sigma$ is the capillary number as is usually defined for a sharp interface. This relation suggests that in order to compare with sharp interface and experimental results one should scale the phase field capillary number by the factor

$$\gamma_K=\frac{2\sqrt{2}K}{3}. \tag{18}$$

We verify this scaling in the numerical experiments.

The dimensionless chemical potential is given by

$$\mu(\phi) = \phi^3 - \phi - K^2\nabla^2\phi. \tag{19}$$

We consider the viscosity ηas a linear function of the order parameter ϕ. That is, if $\eta_- \leqslant \eta \leqslant \eta_+$ and $\eta_c = \eta_-$ we get

$$\eta(\phi) = \frac{\lambda-1}{2}\phi + \frac{\lambda+1}{2}, \tag{20}$$

where $\lambda = \eta_+/\eta_-$ is the viscosity ratio. In this way η gets automatically diffused across the interface with a profile similar to the tanh function.

We focus in this work on the case of constant mobility, $M(\phi) = 1$.

To summarize, the form of Model H that we consider is given by (10), (11), (12), (19), (20) and $M(\phi) = 1$. It is important to note that the Cahn number K (or ξ) is the main parameter for this model. In fact, taking $Pe = O(1/K)$, as argued above, K becomes the only adjustable parameter of the phase-field model as the remaining parameters are of physical nature (Re and Ca).

3. The numerical methodology

We adopt the semi-implicit time scheme used in [3] and extend the 2D adaptive spatial discretization of the Cahn–Hilliard equation in [21] to the current 3D setting of Model H.

3.1. Time discretization

The time scheme for the coupled system is based on an extraction of *linear*, leading order terms and on an implicit treatment of these to remove high order stability constraints without paying the price of iterative nonlinear solvers.

We begin by rewriting the Model H Eqs. (10)–(12). Letting $\varphi_1 = \phi$, we have

$$\frac{\partial\varphi_1}{\partial t} = \frac{1}{Pe}\nabla^2\varphi_2 + g_1(\varphi_1,\varphi_2,\mathbf{u}), \tag{21}$$

$$\varphi_2 = \tau\varphi_1 - K^2\nabla^2\varphi_1, \tag{22}$$

$$\frac{\partial\mathbf{u}}{\partial t} = -\frac{1}{Re}\nabla p + \frac{\bar\eta}{Re}\nabla^2\mathbf{u} + \frac{1}{ReCa}\mu(\varphi_1,\varphi_2)\nabla\varphi_1 + g_2(\varphi_1,\mathbf{u}), \tag{23}$$

$$\nabla\cdot\mathbf{u} = 0, \tag{24}$$

where τ and $\bar\eta$ are constants to be specified later and

$$g_1(\varphi_1,\varphi_2,\mathbf{u}) = \frac{1}{Pe}\nabla^2\mu(\varphi_1,\varphi_2) - \frac{1}{Pe}\nabla^2\varphi_2 - \mathbf{u}\cdot\nabla\varphi_1, \tag{25}$$

$$g_2(\varphi_1,\mathbf{u}) = \frac{1}{Re}\nabla\cdot[\eta(\varphi_1)(\nabla\mathbf{u} + \nabla\mathbf{u}^T)] - \frac{\bar\eta}{Re}\nabla^2\mathbf{u} - \mathbf{u}\cdot\nabla\mathbf{u}. \tag{26}$$

Thus, according to (22), the chemical potential can be expressed by

$$\mu(\varphi_1,\varphi_2) = \varphi_1^3 - (1+\tau)\varphi_1 + \varphi_2. \tag{27}$$

The strategy now is to employ a semi-implicit discretization treating the terms g_1 and g_2 explicitly and all the other terms on the right hand side of (21)–(23) implicitly. As in [3], we adopt here the extrapolated Gear Method, a second order semi-backward difference formula (SBDF), extended to allow for variable time stepping [21]. Leaving the discretization in space for later, the semi-implicit scheme for Model H is given by

$$\frac{\alpha_2\varphi_1^{n+1} + \alpha_1\varphi_1^n + \alpha_0\varphi_1^{n-1}}{\Delta t} = \frac{1}{Pe}\nabla^2\varphi_2^{n+1} + \beta_1 g_1(\varphi_1^n,\varphi_2^n,\mathbf{u}^n) + \beta_0 g_1(\varphi_1^{n-1},\varphi_2^{n-1},\mathbf{u}^{n-1}), \tag{28}$$

$$\varphi_2^{n+1} = \tau\varphi_1^{n+1} - K^2\nabla^2\varphi_1^{n+1}, \tag{29}$$

$$\frac{\alpha_2\mathbf{u}^{n+1} + \alpha_1\mathbf{u}^n + \alpha_0\mathbf{u}^{n-1}}{\Delta t} = -\frac{1}{Re}\nabla p^{n+1} + \frac{\bar\eta}{Re}\nabla^2\mathbf{u}^{n+1} + \frac{1}{ReCa}\mu(\varphi_1^{n+1},\varphi_2^{n+1})\nabla\varphi_1^{n+1} + \beta_1 g_2(\varphi_1^n,\mathbf{u}^n) + \beta_0 g_2(\varphi_1^{n-1},\mathbf{u}^{n-1}), \tag{30}$$

$$\nabla\cdot\mathbf{u}^{n+1} = 0, \tag{31}$$

where $\alpha_0 = \Delta t^2/(\Delta t_0\Delta t_1)$, $\alpha_1 = -\Delta t_1/\Delta t_0$, and $\alpha_2 = (\Delta t_0 + 2\Delta t)/\Delta t_1$, $\beta_0 = -\Delta t/\Delta t_0$ and $\beta_1 = \Delta t_1/\Delta\ t_0$, with $\Delta t = t^{n+1} - t^n$, $\Delta t_0 = t^n - t^{n-1}$, and $\Delta t_1 = \Delta t_0 + \Delta t$. For fixed time step, the coefficients above assume their usual, constant values $\alpha_0 = 1/2$, $\alpha_1 = -2$, and $\alpha_2 = 3/2$, $\beta_0 = -1$ and $\beta_1 = 2$. The stability of this type of semi-implicit discretization has been analyzed recently

by Xu and Tang [37] for the case of some continuum epitaxial growth models. The value of the "stability parameters" τ and $\bar{\eta}$ agrees with that predicted in [37].

In (28)–(31), the phase field is updated first by solving (28) and (29) and then the velocity field is updated using a projection method to solve (30) and (31) as we detail below. To initialize the SBDF, we employ the semi-implicit Euler Method,

$$\frac{\varphi_1^{n+1}-\varphi_1^n}{\Delta t}=\frac{1}{Pe}\nabla^2\varphi_2^{n+1}+g_1(\varphi_1^n,\varphi_2^n,\mathbf{u}^n), \tag{32}$$

$$\varphi_2^{n+1}=\tau\varphi_1^{n+1}-K^2\nabla^2\varphi_1^{n+1}, \tag{33}$$

$$\frac{\mathbf{u}^{n+1}-\mathbf{u}^n}{\Delta t}=-\frac{1}{Re}\nabla p^{n+1}+\frac{\bar{\eta}}{Re}\nabla^2\mathbf{u}^{n+1}+g_2(\varphi_1^n,\mathbf{u}^n)+\frac{1}{ReCa}\mu(\varphi_1^{n+1},\varphi_2^{n+1})\nabla\varphi_1^{n+1} \tag{34}$$

$$\nabla\cdot\mathbf{u}^{n+1}=0. \tag{35}$$

3.2. The projection method

To solve (30) and (31), we employ an incremental pressure-correction scheme based on the variable time step, extrapolated Gear Method [25]. The procedure can be summarized as follows. First, we find an intermediate field $\mathbf{u}^*$

$$\frac{\alpha_2\mathbf{u}^*+\alpha_1\mathbf{u}^n+\alpha_0\mathbf{u}^{n-1}}{\Delta t}=\frac{\bar{\eta}}{Re}\nabla^2\mathbf{u}^*+\frac{1}{ReCa}\mu(\varphi_1^{n+1},\varphi_2^{n+1})\nabla\varphi_1^{n+1}+\beta_1 g_2(\varphi_1^n,\mathbf{u}^n)+\beta_0 g_2(\varphi_1^{n-1},\mathbf{u}^{n-1})-\frac{\nabla p^n}{Re}, \tag{36}$$

with $\mathbf{u}^*=\mathbf{u}^{n+1}$ at the boundary $\partial\Omega$. The intermediate velocity is connected to $\mathbf{u}^{n+1}$ through a pressure increment $q^{n+1}=p^{n+1}-p^n$:

$$\mathbf{u}^*=\mathbf{u}^{n+1}+\frac{\Delta t\nabla q^{n+1}}{\alpha_2 Re}. \tag{37}$$

Applying the incompressibility condition $\nabla\cdot\mathbf{u}^{n+1}=0$ to (37), we obtain a Poisson equation which satisfies a homogeneous Neumann boundary condition for the pressure increment given by

$$\nabla^2 q^{n+1}=Re\frac{\alpha_2}{\Delta t}\nabla\cdot\mathbf{u}^*,\quad \frac{\partial q^{n+1}}{\partial n}=0 \text{ on } \partial\Omega. \tag{38}$$

After solving (38), the updated velocity is obtained from (37).

For sufficiently smooth problems, it can be shown that the pressure-correction scheme based on the second order backward difference formula presents second order accuracy for the velocity and first-order accuracy for the pressure [23]. The loss of accuracy is due to the homogeneous Neumann boundary condition adopted for the pressure-correction Poisson equation which implies that $\nabla p^{n+1}\cdot\mathbf{n}=\nabla p^n\cdot\mathbf{n}=\cdots=\nabla p^0\cdot\mathbf{n}$, thus enforcing a non-physical Neumann boundary condition for the pressure. As a matter of fact, that accuracy behavior is expected to hold if the algorithm is implemented with any A-stable second order time stepping. Since those schemes have an irreducible splitting error of $O(\Delta t^2)$, even using a higher than second order time stepping for approximating the operator $\partial_t-\nu\nabla^2$ does not improve the overall accuracy [22]. Moreover, it can also be shown that the pressure approximation in standard pressure-correction schemes can be at most first-order accurate [24]. In that context, we expect that the solution of (36)–(38) to be second order accurate for the velocity and first order for the pressure.

3.3. Adaptive spatial discretization

Our computational domain is the parallelepiped $\Omega=[A_1,B_1]\times[A_2,B_2]\times[A_3,B_3]$. We employ local mesh refinements to efficiently resolve the thin transition layer of the solution. The composite grid is block-structured and is defined as a hierarchical sequence of nested, progressively finer grid levels [38]. Each level is formed by a set of non-overlapping parallelepipedal grid blocks aligned with the coordinate axes and the refinement ratio between two successive levels is two. Fig. 1 shows an example of such a composite grid with three refinement levels. The mesh is replaced dynamically to ensure that the transition layer is covered with the finest level at all times. Additionally, a remeshing is triggered at every certain fixed number of time steps to "refresh" the composite grid [21].

Ghost cells are appended to each grid block for all levels as well as underneath fine grid blocks to prevent the redefinition of finite difference operators at grid borders and at interior regions which are covered by finer levels. The corresponding values at these ghost cells are obtained from interpolation. Following [21] we use second order polynomial interpolation at grid interfaces and third order interpolation only near a T-junction of two grid blocks of the same level. As the numerical experiments will demonstrate, these interpolations are sufficient to obtain global second order accuracy.

To cover the interfacial layer, we flag for refinement all the cells whose value of the order parameter ϕ is close to zero [21]. By adopting that simpler strategy, the region around the interface will be refined uniformly. Note that for certain problems it

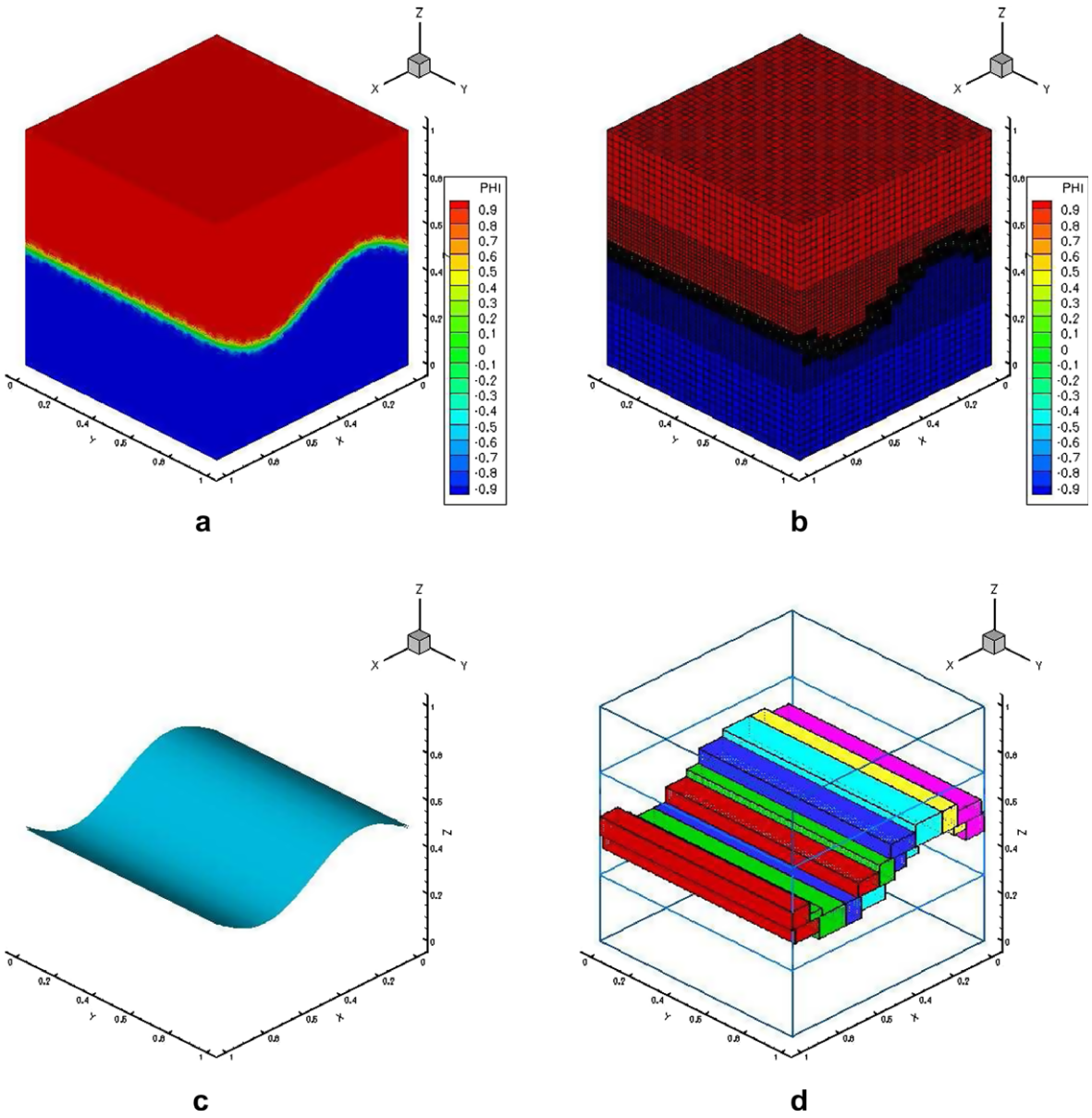

Fig. 1. Example of an adaptive composite grid. (a) A two-phase domain with a thin transition layer represented by the light color, (b) a three-level composite grid, (c) an isosurface of the interface and (d) grid blocks of the finest grid level covering the transition layer (diffuse interface).

would be more efficient to flag cells for refinement accordingly to some error estimator (or distance to the interface) strategy thus having special regions of the flow covered by a greater number of refinement levels than others (e.g. in narrow transition regions where the interface undergoes topological changes). We have postponed the implementation of such optimized strategies to future work and focused our efforts to other components of the methodology. More specifically, in the current implementation, we flag those cell indexes *rst* such that

$$|\phi_{rst}|/\|\phi\|_{\infty} \leqslant \delta_{\text{mesh}}. \tag{39}$$

Typical runs employed $\delta_{\text{mesh}} = 0.95$. With the set of flagged cells, the grids at each level are generated by the algorithm for point clustering of Berger and Rigoutsos [39]. To facilitate the implementation of the projection method, the variables are placed as in a MAC grid. That is, scalar variables such as the pressure, the order parameter, the mobility, and the viscosity are defined at the cell centers while the velocity components are placed at the center of the cell faces as illustrated in Fig. 2.

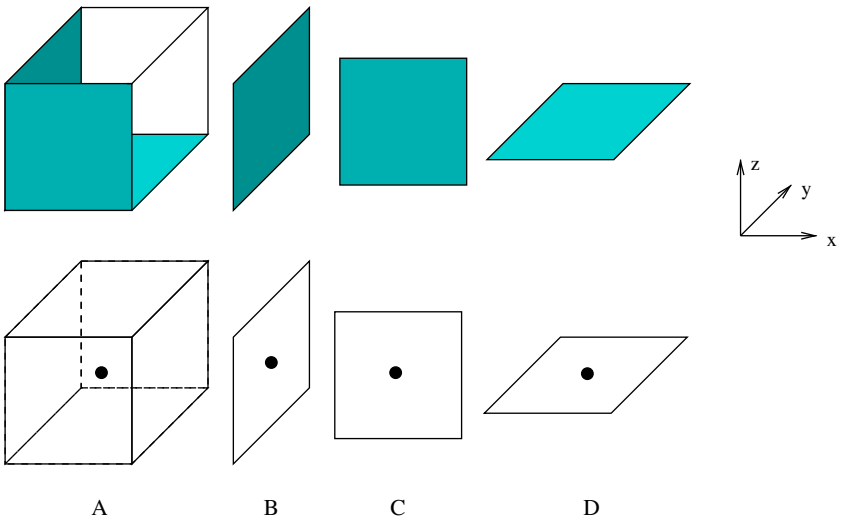

Fig. 2. Placement of variables in a cell for a MAC-style grid. Scalars such as p, φ_1, φ_2, η, and M are located at the cell centers (A). The x, y, and z components of the velocity are placed at the center of the yz face (B), the center of the xz face (C), and the center of the xy face (D), respectively.

3.4. Discrete spatial operators

We use standard second order finite differences to approximate the spatial derivatives. Thus, the discrete gradient G of a scalar quantity such as ϕ is computed by

$$G\phi_{i,j,k} = (D_x\phi_{i-1/2,j,k}, D_y\phi_{i,j-1/2,k}, D_z\phi_{i,j,k-1/2}), \tag{40}$$

where

$$D_x\phi_{i-1/2,j,k} = \frac{\phi_{i,j,k} - \phi_{i-1,j,k}}{\Delta x}, \tag{41}$$

$$D_y\phi_{i,j-1/2,k} = \frac{\phi_{i,j,k} - \phi_{i,j-1,k}}{\Delta y}, \tag{42}$$

$$D_z\phi_{i,j,k-1/2} = \frac{\phi_{i,j,k} - \phi_{i,j,k-1}}{\Delta z}. \tag{43}$$

At coarse cell faces, underneath fine grid patches belonging to the next finer level, the first derivative is defined by the average of the corresponding finer ones.

The discrete divergence operator $\mathbf{D}$ for a vector

$$\mathbf{u}_{i,j,k} = (u_{i-1/2,j,k}, v_{i,j-1/2,k}, w_{i,j,k-1/2}),$$

whose components are located at the center of the cell faces, is given at the cell center by

$$\mathbf{D}\cdot\boldsymbol{u}_{i,j,k} = \frac{u_{i+1/2,j,k} - u_{i-1/2,j,k}}{\Delta x} + \frac{v_{i,j+1/2,k} - v_{i,j-1/2,k}}{\Delta y} + \frac{w_{i,j,k+1/2} - v_{i,j,k-1/2}}{\Delta z}.$$

A discrete Laplacian operator L for cell-centered variables is obtained by composing G and $\mathbf{D}$ i.e., $L\phi_{i,\,j,\,k} = \mathbf{D}\cdot G\phi_{i,j,k}$.

3.5. Solving the resulting linear systems

Due to our semi-implicit time discretization, we can decouple the discrete Model H system. We update first the phase field by solving the linear system corresponding to the fully discrete convective Cahn–Hilliard Eqs. (28) and (29). We then proceed to update the velocity field with the projection method and employing the available ϕ^{n+1} in the surface force term $\mu(\phi)\nabla\phi$. In total, we only solve five linear systems on the composite grid: one for the Cahn–Hilliard equation, three for the components of the intermediate velocity, and one for the pressure. To our knowledge, this is the most efficient time-marching ever proposed for a discretization of Model H on an adaptive mesh.

To solve these linear systems we employ a multi-level multigrid method. Here multilevel refers to the fact that a multigrid method is applied on each level of refinement. Thus, we distinguish between *physical levels* which are the levels of refinement in the composite mesh and *virtual levels* which are the usual levels associated with a multigrid. Given the hierarchical structure of the composite mesh, the virtual levels are just those below the coarsest physical level.

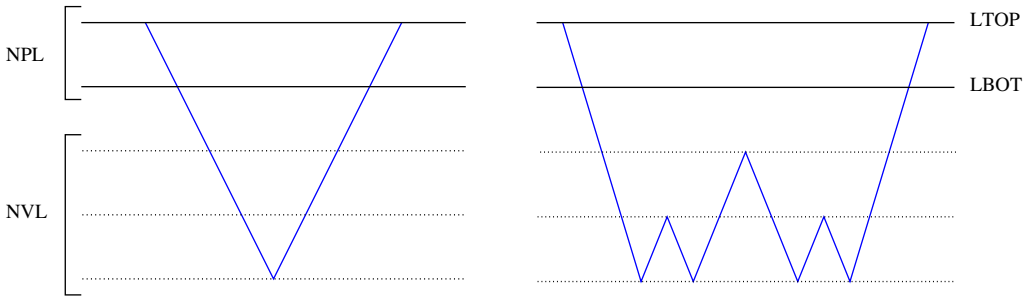

Fig. 3. Comparison of the standard V multigrid cycle (left) and the modified W cycle (right) adopted in this work. NPL = number of physical levels, NVL = number of virtual levels, LTOP = finest physical (refinement) level, and LBOT = coarsest physical level.

Based on preliminary results reported in [40] we adopt a modified W cycle for our multigrid. This adapted W cycle is a V cycle on the physical levels but becomes a W cycle in the virtual levels. Fig. 3 illustrates this strategy. This multigrid appears to give better performance than the standard V cycle when there are four or more virtual levels as is the case for our 3D computations [40].

The application of the multi-level multigrid to solve for the intermediate velocity components and the pressure equation in the projection method is documented in detail in [41]. For Cahn–Hilliard discrete system we have

$$\frac{\alpha_2}{\Delta t}\varphi^{n+1}_{1_{i,j,k}} - \frac{1}{Pe}\mathbf{D}\cdot G\varphi^{n+1}_{2_{i,j,k}} = b_{i,j,k}, \tag{44}$$

$$(\tau - K^2\mathbf{D}\cdot G)\varphi^{n+1}_{1_{i,j,k}} - \varphi^{n+1}_{2_{i,j,k}} = 0, \tag{45}$$

where $b_{i,j,k} = -\alpha_1\varphi^{n}_{1_{i,j,k}}/\Delta t - \alpha_0\varphi^{n-1}_{1_{i,j,k}}/\Delta t + \beta_1 g^{n}_{1_{i,j,k}} + \beta_0 g^{n-1}_{1_{i,j,k}}$. We solve this system with the linear multi-level multigrid method using red–black Gauss–Seidel relaxations in the modified W cycle. Each relaxation sweep merely requires solving a trivial 2×2 linear system. The details of the implementation and multigrid parameters can be found in [21,42].

3.6. Numerical stability

We follow [3] to select Δt. Due to the explicit treatment of the convection term we have a CFL (Courant, Friedrichs and Lewy) stability constraint given by

$$\Delta t_{\mathrm{CFL}} \leqslant \left(\frac{|u|_\infty}{\Delta x} + \frac{|v|_\infty}{\Delta y} + \frac{|w|_\infty}{\Delta z}\right)^{-1}. \tag{46}$$

Due to the coupling between Cahn–Hilliard and Navier–Stokes equations, there is a stability constraint induced by the surface tension term given by [3,49]

$$\Delta t_s \leqslant C_1\sqrt{ReCa}[\min\{\Delta x, \Delta y, \Delta z\}]^{3/2}, \tag{47}$$

where C_1 is a constant. We are using the Gibbs–Thomson boundary condition [33], $\mu(\phi)[\phi] = -\sigma\kappa$, where $[\phi]$ stands for the jump of the order parameter across the interface and κ is the mean curvature and that $\nabla\phi \sim \delta$. With these observations, the stability condition (47) follows from the same arguments as in [49]. With the proposed semi-implicit discretization we find that C_1 could be taken 10 times much larger than that in [3].

Finally, as also noted in [3] there could be a time-stepping constraint due to the viscous term when the interface is very thin (small K) and there is a large viscosity jump:

$$\Delta t_v \leqslant C_2\frac{Re}{\lambda - 1}\min\{\Delta x, \Delta y, \Delta z\}, \tag{48}$$

where C_2 is a constant and can also be chosen 10 times larger than the value for the method in [3]. Our adaptive time-stepping strategy was then selected as

$$\Delta t = \min\{\Delta t_{CFL}, \Delta t_s, \Delta t_v\}. \tag{49}$$

After extensive numerical experimentation, we found that the stability parameters C_1 and C_2 could be chosen to be 100 in our numerical experiments, thus the effective time step was comparable to $\Delta t \leqslant 0.5\Delta t_{CFL}$ in most of our computations.

4. Numerical examples

We now perform a numerical validation of the methodology and demonstrate its efficiency and potential with a set of selected numerical experiments of physical relevance.

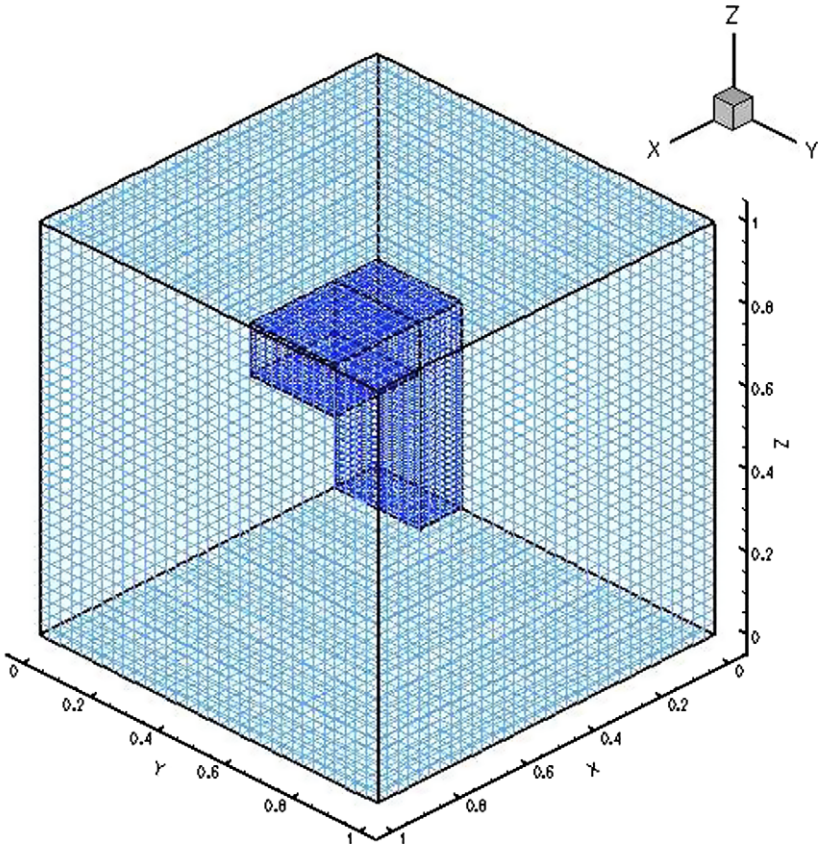

Fig. 4. A two-level composite grid for the accuracy test problem.

4.1. Accuracy check

We first test the accuracy of the adaptive method using a fixed local mesh refinement. This consists of two grid blocks forming an "L" shape that occupy the regions $[0,0.125]\times[0,0.25]\times[0,0.5]$ and $[0.125,0.375]\times[0,0.25]\times[0.375,0.5]$ as shown in Fig. 4. The computational domain is the unit cube. The purpose of this *static-grid* test is to verify that the errors introduced by interpolation and the discretization schemes at coarse–fine level interfaces are correctly controlled to prevent global accuracy degradation. Also, because we have selected the refinements to partially reach the computational domain boundary, the test allows us to verify that the boundary conditions are used properly when filling in ghost cells.

For this test, we construct an exact solution $(\phi_e, \mathbf{u}_e, p_e)$ to the following forced Model H equations:

$$\frac{\partial\phi}{\partial t}+\mathbf{u}\cdot\nabla\phi=\nabla^2\mu(\phi)+F_{\mathrm{CH}}(\phi_e,\mathbf{u}_e), \tag{50}$$

$$\mu(\phi)=\phi^3-\phi-K^2\nabla^2\phi, \tag{51}$$

$$\frac{\partial\mathbf{u}}{\partial t}+\mathbf{u}\cdot\nabla\mathbf{u}=-\nabla p+\nabla^2\mathbf{u}+\mu(\phi)\nabla\phi+\mathbf{F}_{\mathrm{NS}}(\phi_e,\mathbf{u}_e,p_e), \tag{52}$$

$$\nabla\cdot\mathbf{u}=0, \tag{53}$$

in the unit cube $\Omega=[0,1]\times[0,1]\times[0,1]$ and with periodic boundary conditions. Naturally, in (50) and (52)

$$\mathbf{F}_{\mathrm{CH}}(\phi_e,\mathbf{u}_e)=\frac{\partial\phi_e}{\partial t}+\mathbf{u}_e\cdot\nabla\phi_e-\nabla^2\mu(\phi_e), \tag{54}$$

$$\mathbf{F}_{\mathrm{NS}}(\phi_e,\mathbf{u}_e,p_e)=\frac{\partial\mathbf{u}_e}{\partial t}+\mathbf{u}_e\cdot\nabla\mathbf{u}_e+\nabla p_e-\nabla^2\mathbf{u}_e-\mu(\phi_e)\nabla\phi_e, \tag{55}$$

and $\phi(0,\mathbf{x})=\phi_e(0,\mathbf{x})$, $\mathbf{u}(0,\mathbf{x})=\mathbf{u}_e(0,\mathbf{x})$, and $p(0,\mathbf{x})=p_e(0,\mathbf{x})$.

Table 1
Convergence ratios (R) in a two-level composite grid for the forced Model H system. MW stands for the number of multigrid W cycles and $n+1$ means a $n \times n \times n$ uniform grid plus one level of refinement.

$n+1$	Variable	Norm	MW	R
32 + 1	ϕ	$\|\phi - \phi_e\|_2 = 8.113969 \times 10^{-2}$	9	
	p	$\|p - p_e\|_2 = 5.391881 \times 10^{-2}$	7	
	u	$\|u - u_e\|_2 = 4.873936 \times 10^{-3}$	9	
	v	$\|v - v_e\|_2 = 9.129110 \times 10^{-3}$	7	
	w	$\|w - w_e\|_2 = 4.165557 \times 10^{-3}$	8	
64 + 1	ϕ	$\|\phi - \phi_e\|_2 = 2.425453 \times 10^{-2}$	10	3.35
	p	$\|p - p_e\|_2 = 1.587228 \times 10^{-2}$	9	3.40
	u	$\|u - u_e\|_2 = 1.165863 \times 10^{-3}$	12	4.18
	v	$\|v - v_e\|_2 = 1.827253 \times 10^{-3}$	11	5.00
	w	$\|w - w_e\|_2 = 4.286092 \times 10^{-4}$	10	9.72
128 + 1	ϕ	$\|\phi - \phi_e\|_2 = 6.683664 \times 10^{-3}$	10	3.63
	p	$\|p - p_e\|_2 = 4.900852 \times 10^{-3}$	8	3.31
	u	$\|u - u_e\|_2 = 3.738785 \times 10^{-4}$	16	3.12
	v	$\|v - v_e\|_2 = 4.286984 \times 10^{-4}$	15	4.26
	w	$\|w - w_e\|_2 = 6.591865 \times 10^{-5}$	13	6.50

We select (ϕ_e, $\mathbf{u}_e$, p_e) as follows:

$$\phi_e(t,\mathbf{x}) = \sin^3(2\pi x + 2\pi y + 2\pi z + t), \tag{56}$$
$$u_e(t,\mathbf{x}) = \sin^2(2\pi x + 2\pi y + 2\pi z + t), \tag{57}$$
$$v_e(t,\mathbf{x}) = \cos^2(2\pi x + 2\pi y + 2\pi z + t), \tag{58}$$
$$w_e(t,\mathbf{x}) = 1, \tag{59}$$
$$p_e(t,\mathbf{x}) = \cos(2\pi x + 2\pi y + 2\pi z + t). \tag{60}$$

We take $K^2 = 0.01$, and the numerical parameters are $\tau = 2$ and $\bar{\eta} = 1$. Table 1 shows the errors and convergence ratios for this case. The notation "$n+1$" in the first column, stands for a two-level composite grid formed by a $n \times n \times n$ uniform grid (Level 1) plus one additional refinement level (Level 2). The number of multigrid W cycles (MW) to reach truncation error is also displayed. The convergence ratios indicate that the error in the adaptive grid numerical approximation appears to be consistent with that of a second order discretization.

4.2. Deformation of a neutrally buoyant drop

We now consider the deformation of an initially spherical drop under simple shear flow for small Reynolds and capillary numbers. This numerical experiment is intended to serve three purposes: (1) to provide data that we can compare to experimental and theoretical predictions and thus to give further validation and calibration to the model and to our numerical approach, (2) to examine the performance of the semi-implicit discretization in the case of variable viscosity, and (3) to test the adaptive mesh refinements in a difficult geometrical configuration, namely a spherical interface. Although simple in appearance, a spherical interface poses significant challenges to the generation of efficient AMR. The meshing algorithm is based on cuts along the coordinate axes and splits regions with flagged points (for refinement) into rectangular patches. A circular or spherical interface cuts the grid at such an angle that it is necessary to employ a great number of small rectangular patches in order to satisfy the efficiency criterium, namely that the number of cells within a refinement patch should nearly all be flagged cells.

We consider an initially spherical drop of radius $R = 1/4$ with center at $\mathbf{x}_c = (1/2,\ 1/2,\ 1/2)$ in the domain $\Omega = [0,1] \times [0,1] \times [0,1]$. Initially, we specify the phase field as

$$\phi(0,\mathbf{x}) = \tanh\left[\frac{R - \|\mathbf{x} - \mathbf{x}_c\|}{\sqrt{2}\xi}\right], \tag{61}$$

where $\|\mathbf{x} - \mathbf{x}_c\|$ is the Euclidian distance of a point $\mathbf{x}$ to $\mathbf{x}_c$. We take $\xi = 1.5h$, where h is the finest grid size. This choice corresponds to approximately six grid cells covering the equilibrium interface thickness. Fig. 5 displays the initial drop and adaptive grid configuration for four levels of refinement.

For the initial velocity, we choose a linear shear

$$\mathbf{u}(0,x,y,z) = (2z - 1, 0, 0). \tag{62}$$

We maintain the shear by imposing $u = -1$ at $z = 0$ and $u = 1$ at $z = 1$ and assume periodic boundary conditions in the x and y directions. At $z = 0$ and $z = 1$, we take $v = w = 0$ and apply homogeneous Neumann boundary conditions for ϕ and the pressure increment q there.

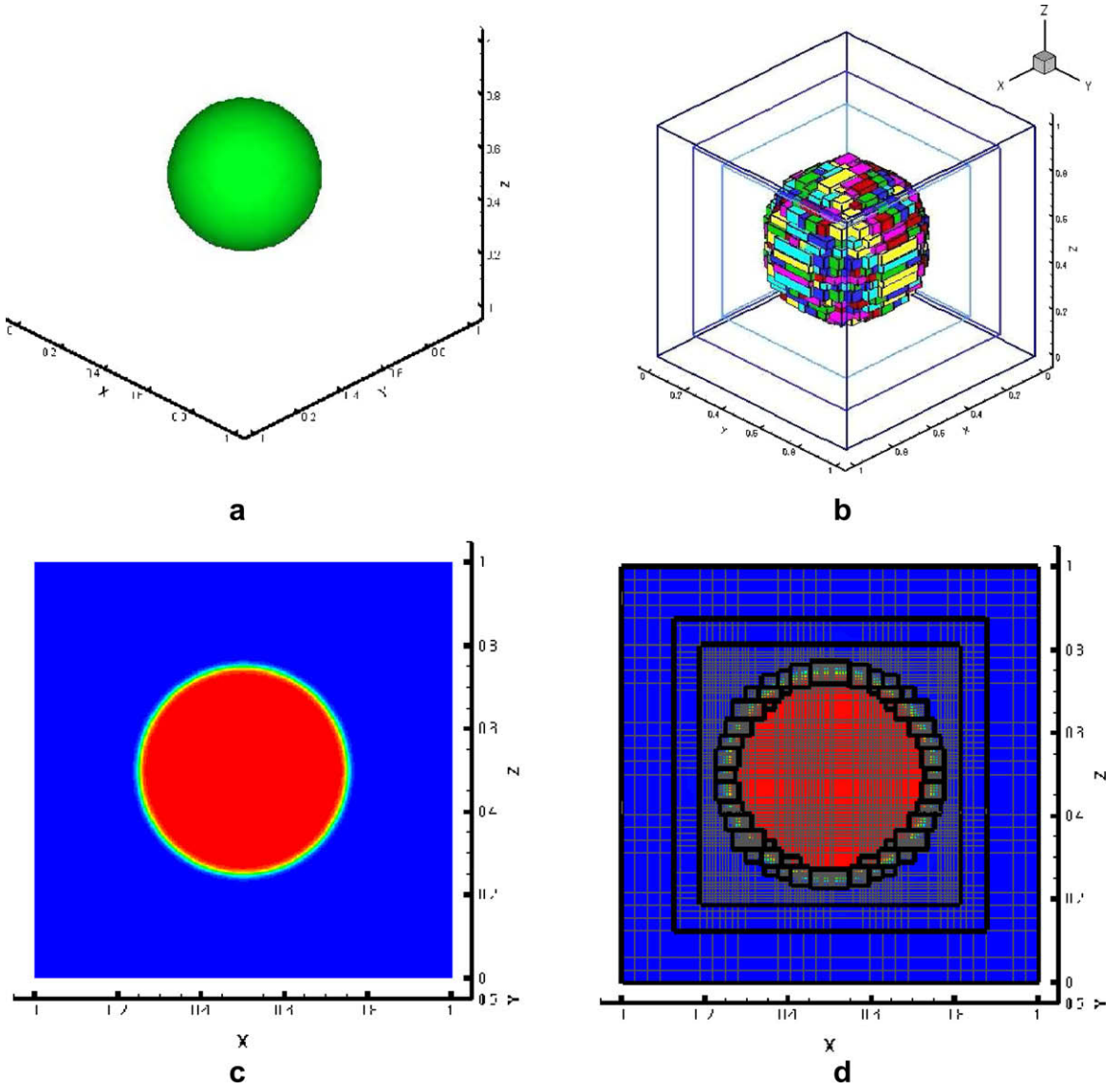

Fig. 5. Initial spherical drop configuration: (a) isosurface $\phi = 0$, (b) grid patches of the finest level surrounding the interface, (c) contour plot of ϕ for a cut at $y = 0.5$, and (d) the same cut showing the four levels of adaptive refinement.

We fix the Reynolds number to $Re = 1$ and take $Pe = 1/K$, where K is the Cahn number (16). We employ four levels of refinement which give a fine grid equivalent to a 256^3 uniform mesh. Given our choice $\xi = 1.5h$, the Cahn number for the four-level composite grid is $K = 1.5/256$.

We perform two series of numerical experiments. In the first one, we consider the same viscosity for the inner and outer fluid ($\lambda = 1$) and take the capillary numbers $Ca = 0.15\gamma_K$, $0.20\gamma_K$, $0.25\gamma_K$, and $0.30\gamma_K$, where γ_K is the Cahn number (interfacial thickness) factor (18). Based on the scaling argument leading to (17), these values of Ca would correspond to sharp interface values Ca^* equal to 0.15, 0.20, 0.25, and 0.30, respectively. One of the purposes of this experiment is to verify that the drop experiences a behavior consistent with these values of Ca^* and that the proposed scaling provides an appropriate calibration of the diffuse-interface model. For the second test, we take $\lambda = 4$ which corresponds to a case where the viscosity of the drop is four times that of the surrounding fluid and $Ca = 0.30\gamma_K$. The numerical parameters in all the numerical experiments are selected as $\tau = 2$ and $\bar{\eta} = \lambda$.

Fig. 6 shows an xz cut of the shear-deformed drop after reaching equilibrium. Under the influence of the flow, the drop assumes the shape of a tilted ellipsoid with a deformation that is a function of the relative effects of surface tension and viscous dissipation, i.e. of the capillary number Ca. The deformation parameter D is obtained in terms of the major and minor axes and the inclination θ is that of the major axis with respect to the horizontal (see for example [43,44]) as indicated in

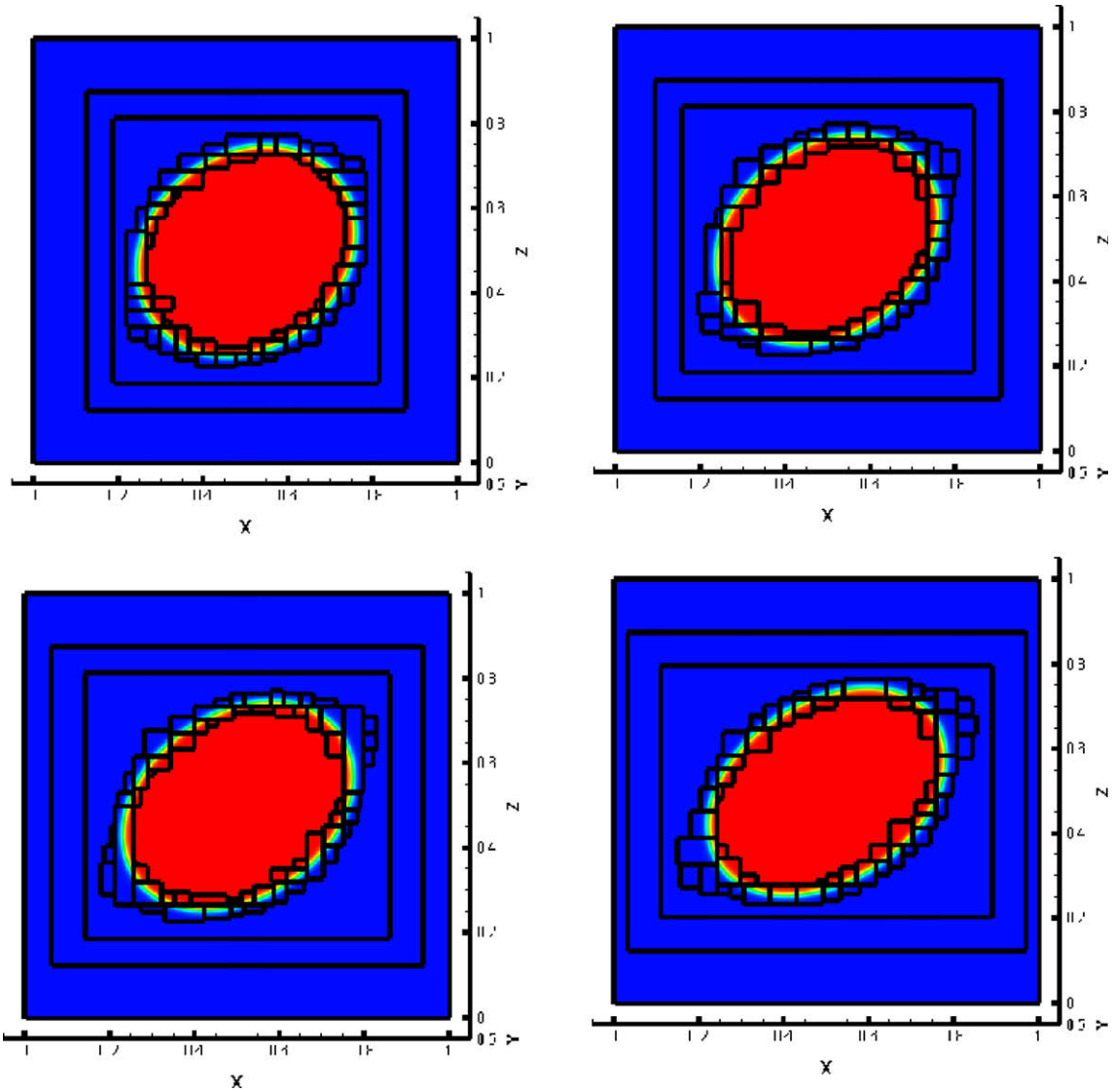

Fig. 6. Drop deformation under shear flow. An xz cut of ϕ and the corresponding adaptive, composite mesh patches. Left to right, top to bottom: $Ca = 0.15\gamma_K$, $Ca = 0.20\gamma_K$, $Ca = 0.25\gamma_K$, and $Ca = 0.30\gamma_K$.

Fig. 7. Equilibrium is determined to have been achieved when the deformation and inclination of the drop are invariant to within numerical accuracy. Table 2 summarizes the values of D and θ for the capillary numbers considered. Note that as Ca is reduced $\theta \to 45°$, i.e. the drop tends to be aligned with the direction of principal extension. Moreover, except for the largest Ca, the deformation has a nearly linear dependence with the capillary number, as Fig. 8 demonstrates. This linear behavior is in agreement with the slender body theory [45] which applies in the limit $Re \to 0$ and $Ca \to 0$. Deviations from this asymptotic theory are expected for the large $Ca^* = 0.30$ [44]. The deformation obtained for $Ca = 0.2\gamma_k$ and $Ca = 0.3\gamma_K$ is within 2% of that reported in [48] (Note, that given our choices of characteristic length, that of the computational domain, and that our relative shear velocity is twice the characteristic velocity, our Ca^* corresponds to half the value in [48]).

We now consider the case of variable viscosity. The initial conditions and setup are the same as for the previous, constant viscosity case but now the viscosity ratio is $\lambda = 4$. The viscosity of the fluid surrounding the drop is four times that of the fluid inside the drop. This particular viscosity ratio is a limit case in the study of flow-induced drop deformation. For $\lambda > 4$ and with an initially spherical drop, it is not possible to deform the drop beyond a modest distortion [44,45]. For sufficiently large λ, if the flow has enough vorticity, the drop will spin almost like a rigid body.

Fig. 9 and Table 3 compare the deformation of the drop with $\lambda = 4$ with the corresponding values for the constant viscosity case ($\lambda = 1$) for a fixed capillary number, $Ca = 0.30\gamma_K$. As expected, the deformation and the inclination of the drop for $\lambda = 4$ are smaller than those for $\lambda = 1$, despite the relatively large Ca. The method performs stably with the time-step criterium (49) for

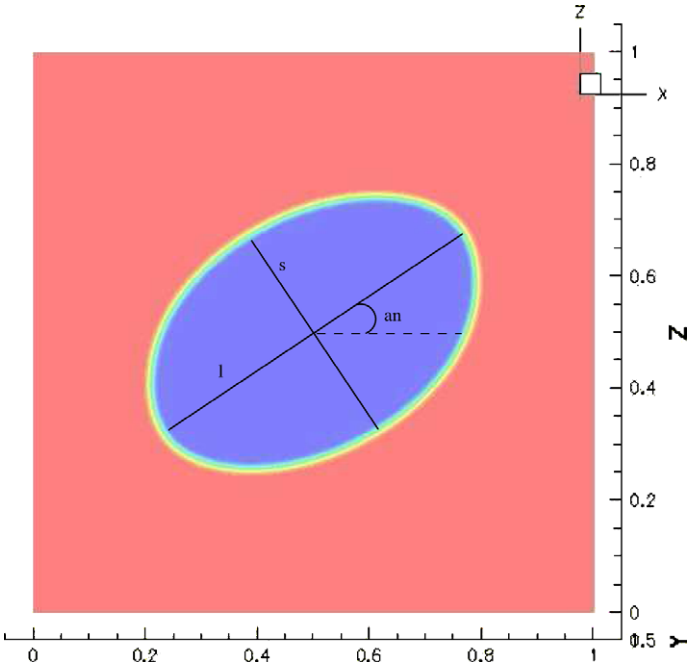

Fig. 7. The axes ℓ and s and the angle of inclination θ in a $y = 0.5$ cut of a drop under shear flow.

Table 2
Deformation D and angle of inclination θ for different Ca. Here ℓ and s are the lengths of the major an minor axis, respectively, and $\gamma_K = \sqrt{2}/256 \approx 5.524 \times 10^{-3}$.

Ca	$D = \frac{\ell - s}{\ell + s}$	θ
$0.15\gamma_K$	0.0959	44°
$0.20\gamma_K$	0.123	43°
$0.25\gamma_K$	0.147	39°
$0.30\gamma_K$	0.184	36°

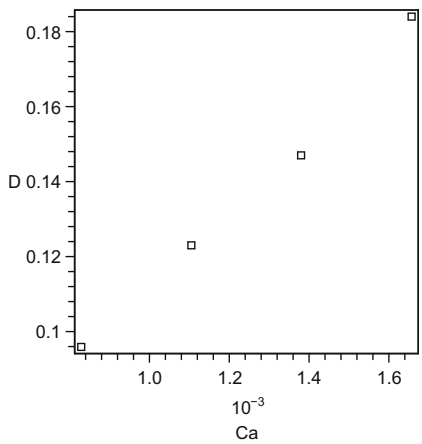

Fig. 8. Drop deformation D under shear flow against Ca.

both $\lambda = 1$ and $\lambda = 4$. The time-step size for $Re = 1$ and the values of Ca considered in these drop deformation experiments is dictated by Δt_s and its size is practically that of a *CFL* condition for most of the simulation time. Thus, the stability constraint

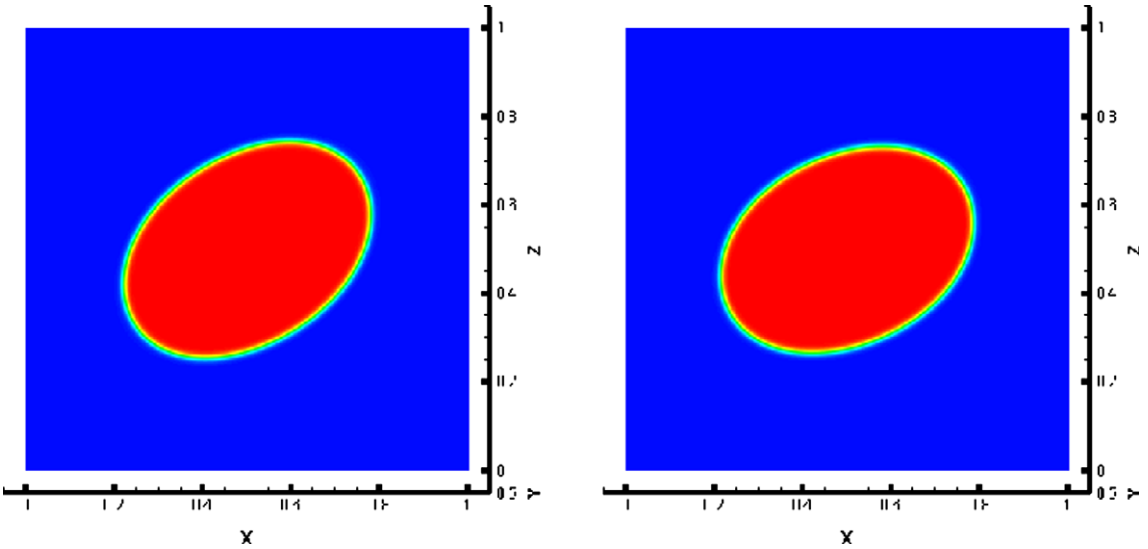

Fig. 9. Comparison of drop deformation under shear flow for viscosity ratios $\lambda = 1$ (left) and $\lambda = 4$ (right) with $Ca = 0.30\gamma_K$.

Table 3
Comparison of the deformation D and inclination angle θ for two viscosity ratios, $\lambda = 1$ and $\lambda = 4$, and $Ca = 0.30\gamma_K$.

Ca	Viscosity	D	θ
$0.30\gamma_K$	$\eta(\phi) = 1$	0.184	36°
$0.30\gamma_K$	$\eta(\phi) = 1.5\phi + 2.5$	0.173	31°

induced by the surface tension term is not entirely removed by the proposed discretization but it is relaxed to a *CFL*-like restriction in practice ($C_1 = 100$). We have compared the performance of the proposed implicit surface tension discretization with one using an explicit, second order (Gear) extrapolation of that term. The latter requires invariably a smaller Δt and this becomes prohibitively small as Re and Ca decrease while Δt for the proposed semi-implicit approach remains of a practical size.

4.3. Kelvin–Helmholtz instability

The Kelvin–Helmholtz (K–H) instability is one of the most fundamental instabilities in incompressible fluids and takes place when two immiscible fluids shear past one another. The motion of the free surface separating the two shearing fluids is dynamically driven by the K–H instability and competing effects of surface tension and viscosity. The investigation of such dynamics is of both fundamental and practical interest. Mixing in the ocean and the atmosphere as well as in engineering fluids such fuels and emulsions, are believed to be induced by instabilities of the K–H type and often these instabilities lead to turbulence [46].

To simulate the K–H instability within Model H, we consider the evolution of a sheared, initially sinusoidal interface. We assume constant viscosity ($\lambda = 1$) and the Reynolds and capillary numbers are selected as $Re = 5000$, $Ca = 200$, respectively. As before $K = 1.5h$, where h is the finest mesh grid size. We employ a composite grid of four levels of refinement, consequently $K = 1.5/256$. We take $Pe = 200$, which remains $O(1/K)$, and the numerical parameter τ is set to 2.

We consider a flow that is independent of the y coordinate to test the ability of the adaptive code to retain the 2D symmetry. We define the initial ϕ in terms of the distance to the curve

$$z_c = 0.01\sin(2\pi x) \tag{63}$$

as follows:

$$\phi(0,x,y,z) = \tanh\left[\frac{3(z-z_c)}{K}\right], \tag{64}$$

for each (x, y, z) in $\Omega = [0,1]\times[0,1]\times[-1,1]$. The initial phase field (64) varies from $\tanh(-3)\approx -0.995$ to $\tanh(3)\approx 0.995$ in a strip of only three computational cells of the finest level covering the transition region.

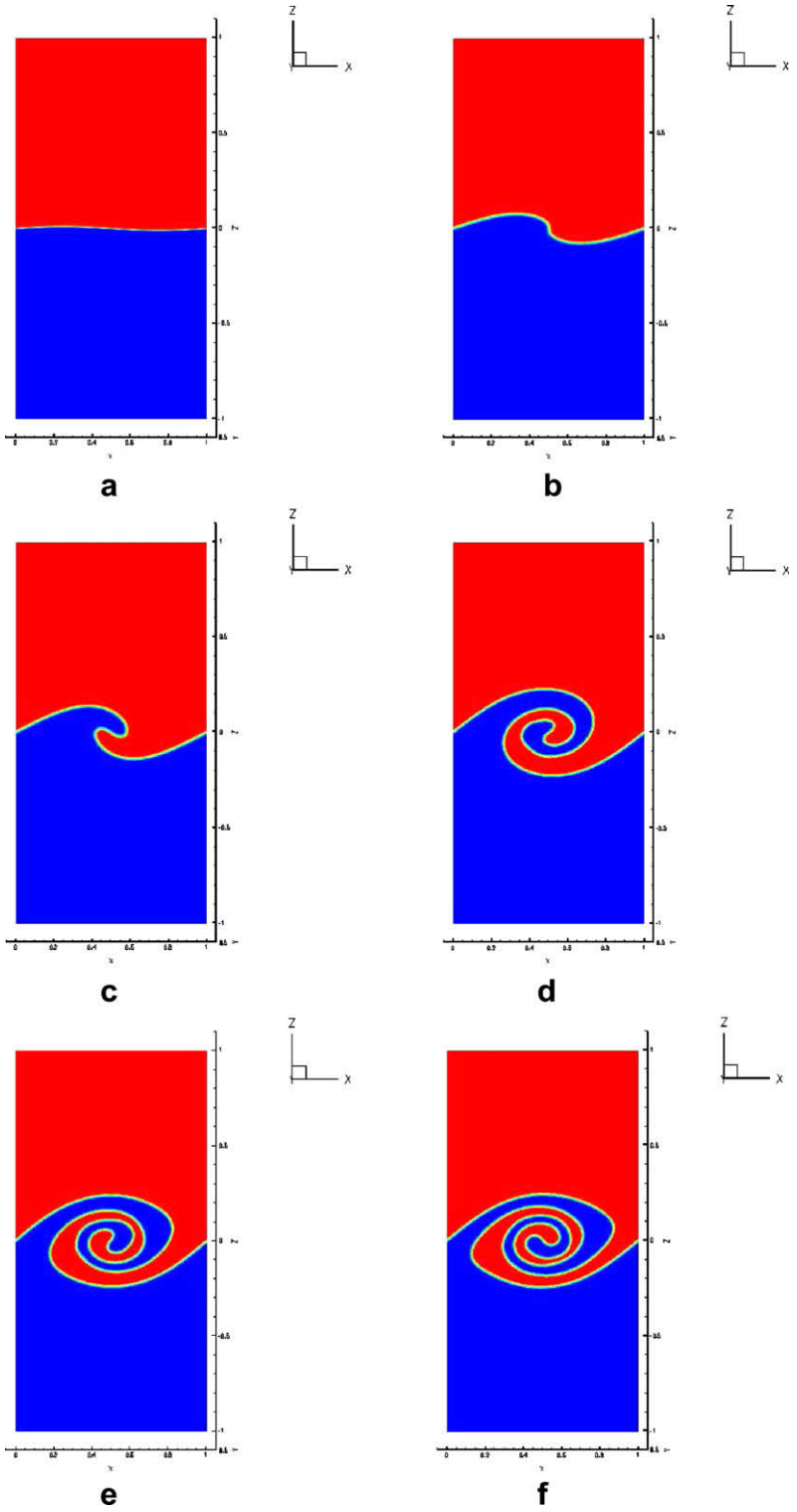

Fig. 10. K–H instability: 2D cut of the order parameter ϕ at different times; (a) $t = 0$, (b) $t = 0.65$, (c) $t = 0.87$, (d) $t = 1.43$, (e) $t = 1.63$, and (f) $t = 1.83$.

We specify an initial shear flow in the x direction by

$$\mathbf{u}(0, x, y, z) = (\tanh[25(z - z_c)], 0, 0) \tag{65}$$

and impose $u = \pm 1$ and $v = w = 0$ at $z = \pm 1$ and periodic boundary conditions in the x and y directions.

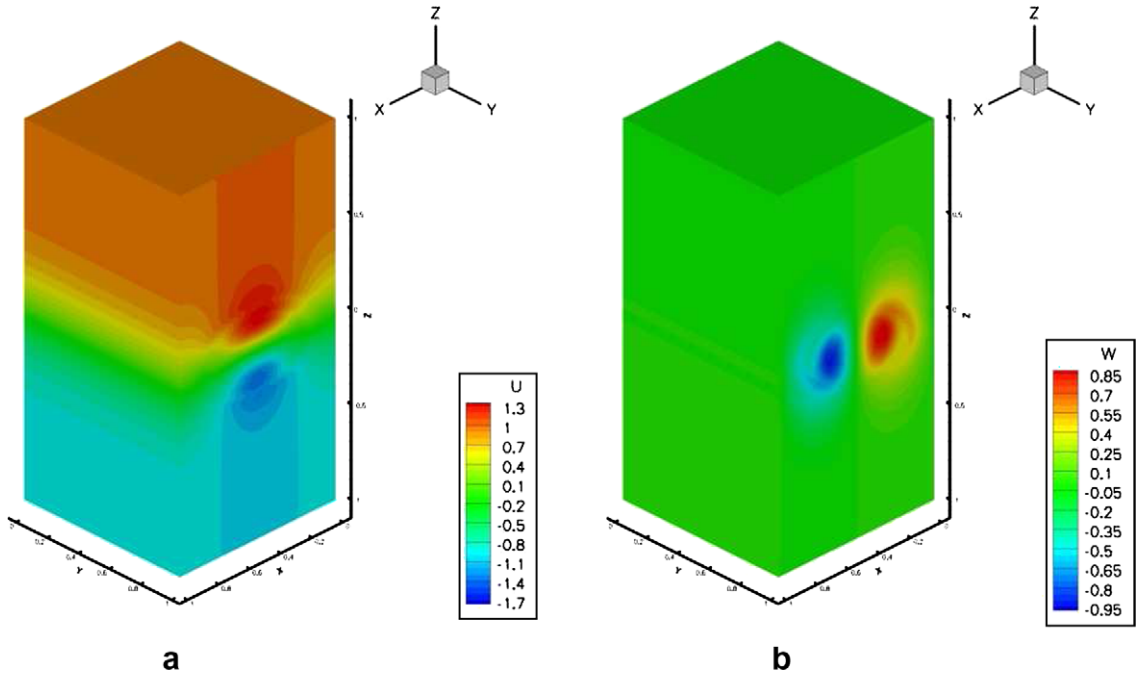

Fig. 11. K–H instability: (a) stream-wise (u) velocity component and (b) normal-wall (w) velocity component at $t = 1.69$.

Fig. 10 shows a two dimensional cut of the order parameter ϕ at different times to illustrate the evolution of the shearing interface. Early in the dynamics, the flow sweeps the initial interfacial vorticity into the center and as vorticity accumulates at this point, the surface begins to steepen. Roll-up follows and the surface evolves into a spiral with a "cat eye" shape typically observed in the experiments [46]. A look at the stream-wise and normal-wall velocity components at late time of the evolution (Fig. 11) indicates two strong centers of vorticity driving up the dynamics. Throughout the entire motion, the finest level of the adaptive mesh covers the diffuse interface and the 2D geometry of the motion is retained as Fig. 12 demonstrates. The dynamics of the rolling sheet are consistent with those obtained in 2*D* numerical simulations using immersed boundary type methods [41,47].

4.4. Coalescence of deformable drops

For our final test, we consider an initial configuration of two identical spherical drops of radius $R = 1/5$, separated a small distance apart. The drops are going to be brought into a glancing collision by a shear flow. The problem of flow-induced coalescence has received considerable recent attention due to the role that this process plays in the formation of polymer blends, which is currently the major route to new polymeric materials with desired macroscopic properties. The understanding of the conditions for coalescence and their dependence on fluid and flow properties is critical for controlling this process.

In the context of phase-field models, Barosan et al. [20] considered 2D flow-induced drop coalescence to test the capabilities of their modern, adaptive mortar elements method. As indicated earlier, there are few works on adaptive, phase field, *conservative* methods and the challenging coalescence simulations in [20] are one of the very few existing examples. For our simulation we have chosen to use the same setup as in [20] but in 3D. One more important difference is that we retain inertial effects (full Navier–Stokes equations) whereas in [20] a Stokes approximation ($Re = 0$) is used. This numerical experiment offers the opportunity to test the proposed phase-field based method through an interfacial topological change and to examine the conservation of volume during that singular transition.

Initially, the center of the drops is at

$$\mathbf{x}_1 = (0.299, 0.5, 0.45), \tag{66}$$

$$\mathbf{x}_2 = (0.701, 0.5, 0.55), \tag{67}$$

respectively and the computational domain is $\Omega = [0,1] \times [0,1] \times [0,1]$. The initial order parameter is given by

$$\phi(0,\mathbf{x}) = \begin{cases} \tanh\left(\frac{R-\|\mathbf{x}-\mathbf{x}_1\|}{\sqrt{2}K}\right) & \text{for } \|\mathbf{x}-\mathbf{x}_1\| < R + 2\sqrt{2}K, \\ \tanh\left(\frac{R-\|\mathbf{x}-\mathbf{x}_2\|}{\sqrt{2}K}\right) & \text{for } \|\mathbf{x}-\mathbf{x}_2\| < R + 2\sqrt{2}K. \end{cases} \tag{68}$$

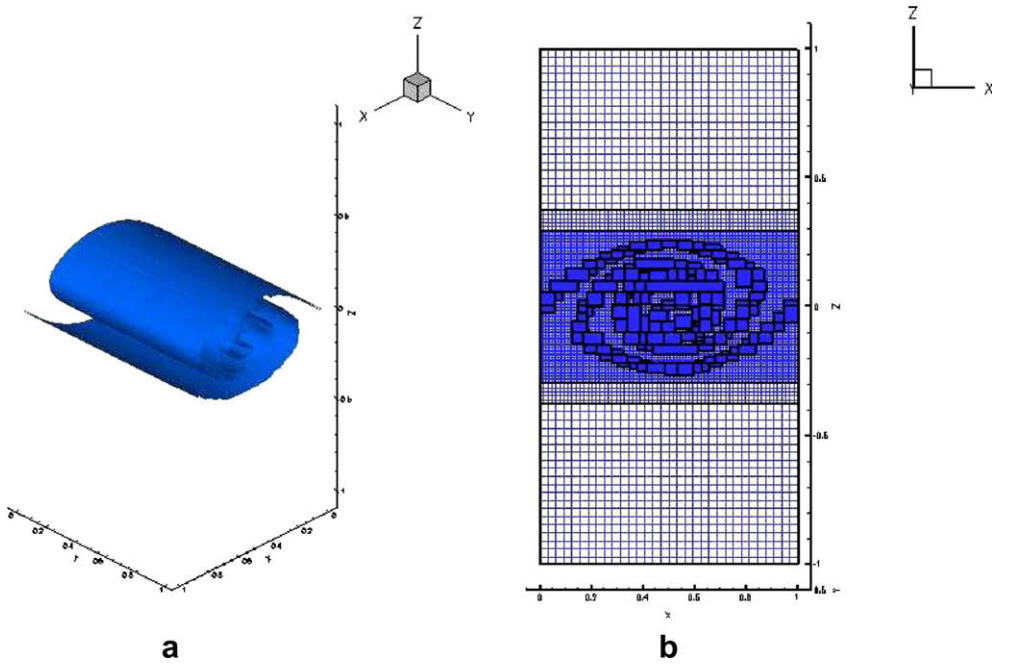

Fig. 12. K–H instability: (a) isosurface at $t = 1.69$ and (b) a $y = 0.5$ cut of the four level, composite adaptive mesh at $t = 1.69$.

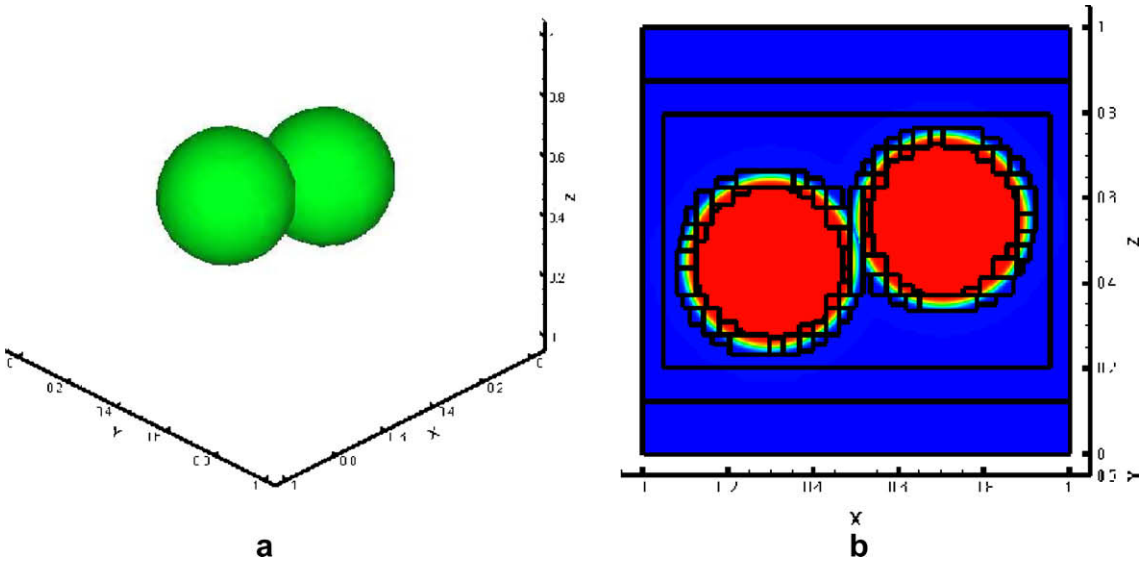

Fig. 13. Flow-induced drop coalescence: (a) isosurface $\phi = 0$ at $t = 0$ and (b) a $y = 0.5$ cut of the four level, composite adaptive mesh at $t = 0$.

The initial velocity is the simple linear shear flow (62). We take $\lambda = 1$ (viscosity ratio equal one) and $Ca = 0.001$ as in [20] and $Re = 0.1$. We employ four levels of refinement and $K = 1.4/256$. Fig. 13 shows the initial configuration of the drops and the adaptive mesh refinement, represented as grid patches (with black perimeters) corresponding to the different adaptive levels.

A sequence of the flow dynamics is depicted in Fig. 14 where a 2D, xz plane cut is chosen to better visualize the drop interaction. Once all the fluid from the initially thin gap between the two drops is drained the drops coalesce and a single drop is formed. Eventually, this drop evolves into an ellipsoid reaching a steady state that balances the shear stress, surface tension, and viscous dissipation. Fig. 15 shows in a 2D cut the adaptive mesh patches of the four-level composite

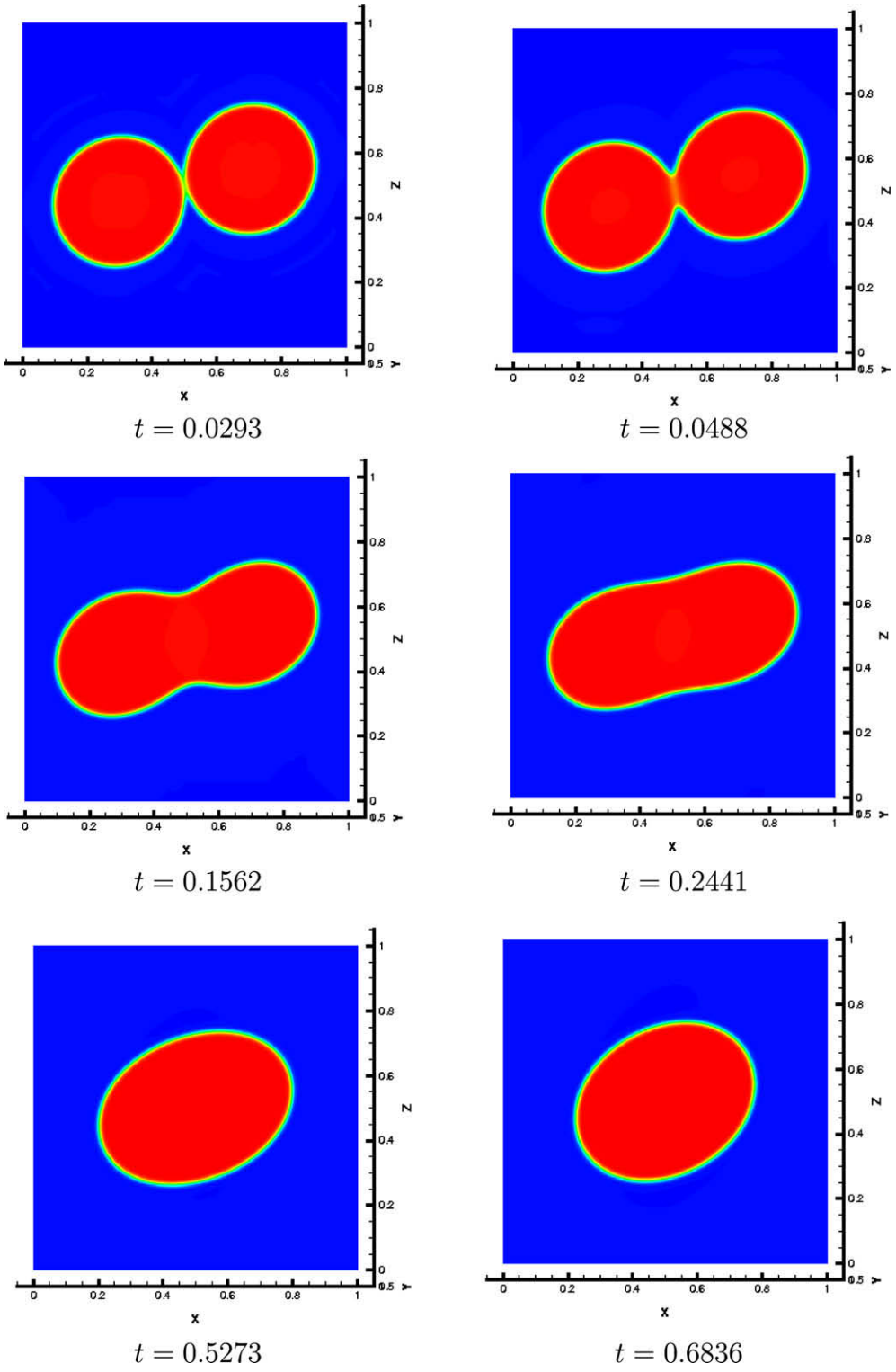

Fig. 14. Flow-induced drop coalescence dynamics. 2D, *xz* cuts of the order parameter.

grid as well as isosurfaces ($\phi = 0$) of the order parameter at two flow instants. The finest refinement level accompanies the fluid interfaces and the interaction region until the order parameter reaches a nearly uniform value inside the coalesced drop. Throughout the entire computation the mean of the order parameter and the volume of the drops have a

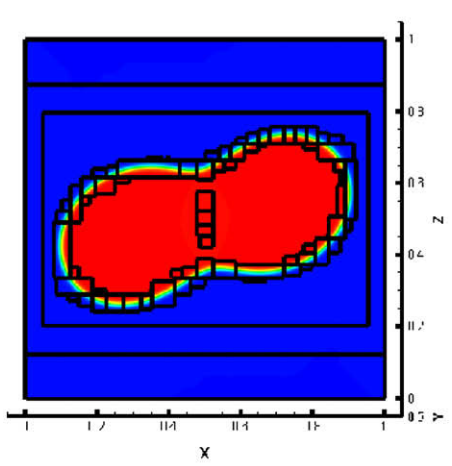

AMR patches at $t = 0.1562$

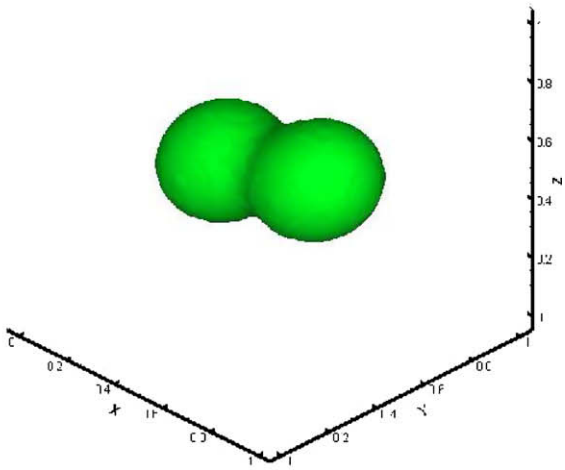

Isosurface $\phi = 0$ at $t = 0.1562$

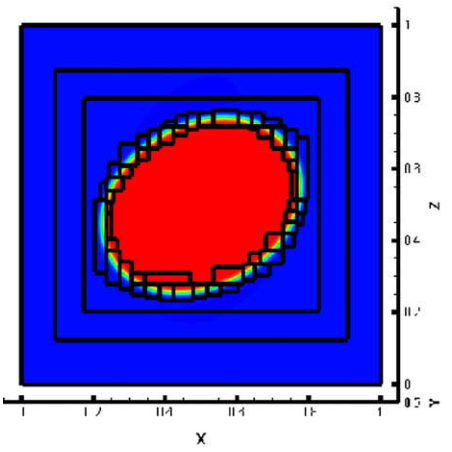

AMR patches at $t = 0.6836$

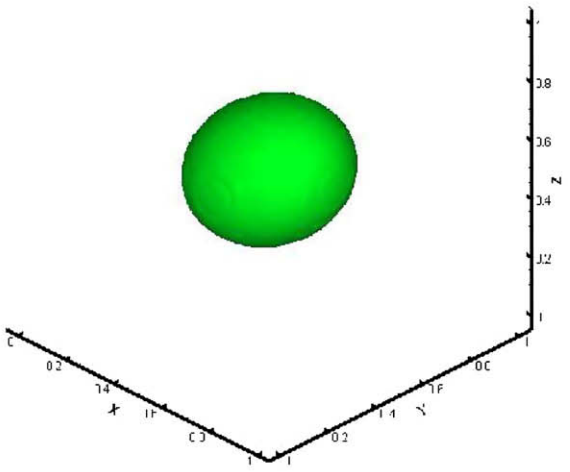

Isosurface $\phi = 0$ at $t = 0.6836$

Fig. 15. Flow-induced drop coalescence. 2D cut of the four-level adaptive mesh patches and isosurfaces $\phi = 0$ at two different times.

variation of only 0.09%. Fig. 16 compares the number of computational cells of the four-level adaptive grid, as it evolves in time, against a corresponding uniform grid. Even with only four levels of refinement, the composite grid uses only nearly a quarter of the computational cells required by a uniform grid with the same resolution. Of course, the savings increase as the number of refinement levels is increased, leading in the limit to an asymptotic linear scaling of the computational work.

5. Conclusions

We presented a fully adaptive 3D computational strategy for the simulation of multi-phase flows described by conservative phase-field models such as Model H. The proposed numerical methodology combines efficiently local adaptive mesh refinements, a variable time-stepping semi-implicit time discretization, and the use of linear multi-level multigrid solvers; only five linear solvers are required per time-step. The discretization relaxes high order stability constraints and does not carry the cost of nonlinear iterative solvers used in fully implicit discretizations. The adaptive methodology is constructed from scratch to allow a systematic investigation of the key aspects of AMR in a conservative phase-field model setting: flagging, interpolation, and multi-level composite grid solvers. The efficiency, capabilities and potential of the methodology were demonstrated with illustrative examples of drop deformation, Kelvin–Helmholtz instability, and flow-induced drop coalescence.

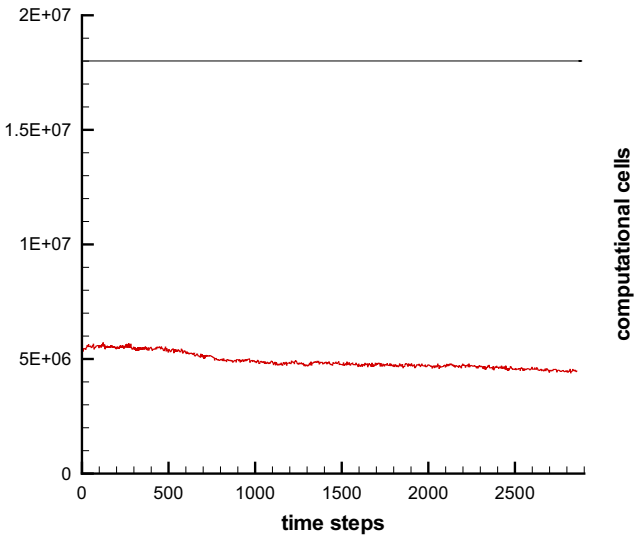

Fig. 16. Variation in time of the number of computational cells of the adaptive grid (red) and a comparison with a corresponding uniform grid (black). (For interpretation of the references to colour in this figure legend, the reader is referred to the web version of this article.)

Acknowledgments

Partial support for this research was provided by the NSF under Grant No. DMS 0609996 (HDC), by FAPESP under Grant Nos. 04/13781-1 and 06/57099-5, and byCNPq Grant No. 307348/2008-3 (AMR). The authors would like to acknowledge the hospitality of the Department of Mathematics at UCSB and of the Departamento de Matemática Aplicada at USP during the three-month visit of the authors (R.L.N and A.M.R. visited UCSB and H.D.C. visited USP) in the course of which part of this research was conducted. The authors are also grateful to director and staff of LACIT – Laboratório de Ciências Térmicas da UTFPR for generously allowing use of their facilities.

References

[1] R. Chella, V. Viñals, Mixing of a two-phase fluid by a cavity flow, Phys. Rev. E 53 (1996) 3832.
[2] D. Jacqmin, Calculation of two-phase Navier–Stokes flows using phase-field modeling, J. Comput. Phys. 155 (1999) 96–127.
[3] V.E. Badalassi, H.D. Ceniceros, S. Banerjee, Computation of multiphase systems with phase field models, J. Comput. Phys. 190 (2003) 371–397.
[4] V.E. Badalassi, H.D. Ceniceros, S. Banerjee, Gravitational effects on structural development in quenched complex fluids, Ann. NY Acad. Sci. 1027 (2004) 371–382.
[5] J. Kim, K. Kang, J. Lowengrub, Conservative multigrid methods for Cahn–Hilliard fluids, J. Comput. Phys. 193 (2004) 511–543.
[6] J. Kim, K. Kang, J. Lowengrub, Conservative multigrid methods for ternary Cahn–Hilliard systems, Commun. Math. Sci. 2 (2004) 53–77.
[7] F. Boyer, L. Chupin, P. Fabrie, Numerical study of viscoelastic mixtures through a Cahn–Hilliard flow model, Eur. J. Mech. B/Fluids 23 (2004) 759–780.
[8] P. Yue, J.J. Feng, C. Liu, J. Shen, A diffuse-interface method for simulating two-phase flows of complex fluids, J. Fluid Mech. 515 (2004) 293–317.
[9] P. Yue, J.J. Feng, C. Liu, J. Shen, Viscoelastic effects on drop deformation in steady shear, J. Fluid Mech. 540 (2005) 427–437.
[10] P. Yue, J.J. Feng, C. Liu, J. Shen, Diffuse-interface simulations of drop-coalescence and retraction in viscoelastic fluids, J. Non-Newtonian Fluid Dynam. 129 (2005) 163–176.
[11] P. Yue, C. Zhou, J.J. Feng, C.F. Ollivier-Gooch, H.H. Hu, Phase-field simulations of interfacial dynamics in viscoelastic fluids using finite elements with adaptive meshing, J. Comput. Phys. 219 (2006) 47–67.
[12] D.M. Anderson, G.B. McFadden, A.A. Wheeler, Diffuse-interface methods in fluid mechanics, Annu. Rev. Fluid Mech. 30 (1998) 139.
[13] S.D. Poisson, Nouvelle Théorie de l'Action Capillaire, Bachelier, Paris, 1831.
[14] J.C. Maxwell, Capillary action, in: Encyclopaedia Britannica, 9th ed., 1876, reprinted in The Scientific Papers of James Clerk Maxwell, Dover, New York, 1951.
[15] J.W. Gibbs, On the equilibrium of heterogeneous substances, Trans. Conn. Acad. 3 (1876) 108–248 (reprinted in The Scientific Papers of J. Willard Gibbs, Longman, Green, London, 1906).
[16] Lord Rayleigh, On the theory of surface forces-II. Compressible fluids, Philos. Mag. 33 (1892) 209.
[17] J.D. van der Waals, The thermodynamic theory of capillarity under the hypothesis of a continuous variation of density, Verhandel. Konink. Akad. Weten. (Amsterdam) 1 (1893) 8 (originally published in Dutch. Translation published by J.S. Rowlinson, J. Stat. Phys. 20 (1979) 200–244).
[18] J. Zhu, L.Q. Chen, J. Shen, V. Tikare, Coarsening kinetics from a variable-mobility Cahn–Hilliard equation: application of a semi-implicit Fourier spectral method, Phys. Rev. E 60 (4) (1999) 3564–3572.
[19] H. Garcke, M. Rumpf, U. Weikard, The Cahn–Hilliard equation with elasticity: finite element approximation and qualitative studies, Interfaces Free Bound. 3 (2001) 101–118.
[20] I. Barosan, P.D. Anderson, H.E.H. Meijer, Application of mortar elements to diffuse-interface methods, Comput. Fluids 35 (2006) 1384–1399.
[21] H.D. Ceniceros, A.M. Roma, A nonstiff, adaptive mesh refinement-based method for the Cahn–Hilliard equation, J. Comput. Phys. 225 (2) (2007) 1849–1862.
[22] J.L. Guermond, P. Minev, Jie Shen, An overview of projection methods for incompressible flows, Comput. Methods Appl. Mech. Eng. 195 (2006) 60116045.
[23] J.L. Guermond, Un résultat de convergence d'ordre deux en temps pour l'approximation des équations de NavierStokes par une technique de projection incrémentale, M2AN Math. Model. Numer. Anal. 33 (1) (1999) 169189.

[24] J.C. Strikwerda, Y.S. Lee, The accuracy of the fractional step method, SIAM J. Numer. Anal. 37 (1) (1999) 3747.
[25] H.D. Ceniceros, A.M. Roma, A. Silveira-Neto, M.M. Villar, A robust, fully adaptive hybrid level-set/front-tracking method for two-phase flows with an accurate surface tension computation, Commun. Comput. Phys. 8 (2010) 51–94.
[26] J.J. Tapia, P. Gilberto López, Adaptive pseudospectral solution of a diffuse interface model, J. Comput. Phys. 224 (2009) 101–117.
[27] P.C. Hohenberg, B.I. Halperin, Theory of dynamic critical phenomena, Rev. Mod. Phys. 49 (3) (1977) 435.
[28] J.W. Cahn, J.E. Hilliard, Free energy of a nonuniform system I, J. Chem. Phys. 28 (1958) 258.
[29] J.W. Cahn, J.E. Hilliard, Free energy of a nonuniform system III, J. Chem. Phys. 31 (1959) 688.
[30] C. Zhou, P. Yue, J.J. Feng, C.F. Ollivier-Gooch, H.H. Hu, 3D phase-field simulations of interfacial dynamics in Newtonian and viscoelastic fluids, J. Comput. Phys. 229 (2010) 498–511.
[31] H. Lee, J.S. Lowengrub, J. Goodman, Modeling pinchoff and reconnection in a Hele-Shaw cell. I. The models and their calibration, Phys. Fluids 14 (2) (2002) 492.
[32] V.V. Khatavkar, P.D. Anderson, H.E.H. Meijer, On scaling of diffuse-interface models, Chem. Eng. Sci. 61 (2006) 2364–2378.
[33] A.J. Bray, Theory of phase-ordering kinetics, Adv. Phys. 43 (3) (1994) 357–459.
[34] M.E. Gurtin, D. Polignone, J. Viñals, Two-phase binary fluids and immiscible fluids described by an order parameter, Math. Models Methods Appl. Sci. 6 (6) (1996) 815.
[35] J. Lowengrub, L. Truskinovsky, Quasi-incompressible Cahn–Hilliard fluids and topological transitions, Proc. R. Soc. London A 454 (1998) 2617.
[36] F. Boyer, A theoretical and numerical model for the study of incompressible mixture flows, Comput. Fluids 31 (1) (2002) 41.
[37] C. Xu, T. Tang, Stability analysis of large time-stepping methods for epitaxial growth models, SIAM J. Numer. Anal. 44 (4) (2006) 1759–1779.
[38] M.J. Berger, P. Colella, Local adaptive mesh refinement for shock hydrodynamics, J. Comput. Phys. 82 (1989) 64–84.
[39] M.J. Berger, I. Rigoutsos, An algorithm for point clustering and grid generation, IEEE Trans. Syst. Man Cybernet. 21 (5) (1991) 1278–1286.
[40] R.L. Nós, A.M. Roma, H.D. Ceniceros, Solução de equações diferenciais parciais elípticas por técnicas multinível-multigrid em malhas tridimensionais bloco-estruturadas com refinamento localizado, in: Anais do XXVIII Congresso Nacional de Matemática Aplicada e Computacional, São Paulo, 2005.
[41] H.D. Ceniceros, A.M. Roma, Study of the long-time dynamics of a viscous vortex sheet with a fully adaptive non-stiff numerical method, Phys. Fluids 16 (12) (2004) 4285–4318.
[42] R.L. Nós, Simulações de escoamentos tridimensionais bifásicos empregando métodos adaptativos e modelos de campo de fase, Ph.D. Thesis, Universidade de São Paulo, Brasil, 2007.
[43] J.M. Rallison, The deformation of small viscous drops and bubbles in shear flows, Annu. Rev. Fluid Mech. 16 (1984) 45–66.
[44] H.A. Stone, Dynamics of drop deformation and breakup in viscous fluids, Annu. Rev. Fluid Mech. 26 (1994) 65–102.
[45] G.I. Taylor, The viscosity of a fluid containing small drops of another fluid, R. Soc. London Proc. Ser. A 138 (1932) 41–48.
[46] P. Atsavapranee, M. Gharib, Structures in stratified plane mixing layers and the effects of cross-shear, J. Fluid Mech. 342 (1997) 53–86.
[47] T.Y. Hou, Z. Shi, An efficient semi-implicit immersed boundary method for the Navier–Stokes equations, J. Comput. Phys. 227 (2008) 8968–8991.
[48] V. Sibillo, G. Pasquariello, M. Simeone, V. Cristini, S. Guido, Drop deformation in microconfined shear flow, Phys. Rev. Lett. 97 (2006) 054502.
[49] M. Kang, R.P. Fedkiw, X. Liu, A boundary condition capturing method for multiphase incompressible flow, J. Sci. Comput. 15 (2000) 323–360.